COMMUNICATION

Check for updates

Imidazolium ligand-modified Cu_2O catalysts for enhancing C_{2+} selectivity in CO_2 electroreduction *via* local *CO enrichment†

Rongzhen Chen,[a] Ling Zhang[a] and Yuhang Li (iD) *[ab]

Electrochemical CO_2 reduction (CO_2RR) to synthesize multicarbon products is a critical route for sustainable CO_2 utilization, yet achieving high selectivity and current density simultaneously remains challenging. While enhancing *CO coverage on catalysts is pivotal for promoting C–C coupling, the dynamic competition between intermediate enrichment and microenvironment regulation necessitates innovative strategies. Here, we employ surface ligand engineering to construct a tunable hydrophobic microenvironment on Cu_2O catalysts, using imidazolium-based ionic liquids with alkyl side chains of varying lengths. The optimized OMIm-Cu_2O catalyst achieves a C_{2+} selectivity of 63.3% in alkaline media and 30.7% in acidic media. Mechanistic studies reveal that hydrophobic long-chain ligands elevate local *CO concentration, facilitating efficient C–C coupling. This work highlights microenvironment modulation as a viable pathway to bridge the gap between high efficiency and industria–current–density performance in CO_2RR.

Keywords: Electrochemical CO_2 reduction; C_{2+} product selectivity; Copper-based catalysts; *CO concentration.

1. Introduction

Electrochemical CO_2 reduction reaction (CO_2RR) driven by renewable electricity to synthesize C_{2+} products represents a pivotal pathway for CO_2 resource utilization. C–C coupling, the rate-determining step in generating C_{2+} products, is directly constrained by the *CO coverage on the catalyst surface.[1–3] Consequently, various strategies have been employed to enhance the local *CO concentration and promote C_{2+} product formation, including size and morphology control,[4,5] surface doping,[6,7] and oxidation modulation.[8,9] Nam *et al.* reported

[a] Key Laboratory for Ultrafine Materials of Ministry of Education, Shanghai Engineering Research Center of Hierarchical Nanomaterials, School of Materials Science and Engineering, East China University of Science & Technology, Shanghai 200237, China. E-mail: yuhangli@ecust.edu.cn
[b] Department of Chemical Engineering, School of Chemistry and Chemical Engineering, Shanghai Jiao Tong University, Shanghai 200240, China
† Electronic supplementary information (ESI) available. See DOI: https://doi.org/10.1039/d5im00052a

that Cu electrodes with a mesoporous structure can enrich *CO intermediates within the mesopores, thus enhancing the selectivity toward C_{2+} products.[10] Likewise, Jung *et al.* demonstrated that porous Cu/Cu_2O aerogel catalysts yield a higher *CO concentration around the catalyst surface compared to nanoparticle or planar film catalysts.[11] Notably, current technological systems still face challenges in simultaneously achieving high faradaic efficiency (FE >70%) and ultra-high current densities (>600 mA cm^{-2}), primarily due to the dynamic competition between mass transport limitations and the decay of electrochemically active sites.

Surface ligand engineering offers a precise means of controlling CO_2RR selectivity by modulating the catalyst's electronic structure, steric hindrance, and local microenvironment. Ligands can alter the adsorption strength of intermediates (*e.g.*, *COOH, *CO) *via* electronic effects, thereby directing the product pathway.[12,13] In addition, steric hindrance can suppress the hydrogen evolution reaction or adjust product distribution,[14–17] while optimization of the local microenvironment enhances target product activity by increasing reactant concentration or suppressing side reactions.[14,15,18] Furthermore, ligands can stabilize intermediates through chemical interactions (such as hydrogen bonding to lock *COOH) or enable dynamic restructuring (as observed in MOF-derived catalysts) to adapt to reaction conditions, facilitating efficient C–C coupling and selective product formation.

Herein, we constructed a tunable hydrophobic microenvironment *via* surface ligand engineering to enrich *CO intermediates locally and promote C–C coupling, thereby enhancing the selectivity toward C_{2+} products. Using ionic liquids as precursors, we synthesized a series of copper-based catalysts modified with imidazolium ligands bearing alkyl side chains of varying lengths. Characterization by ATR-FTIR, XPS, and EDS elemental mapping confirmed the successful surface modification of Cu_2O by the ligands. In both acidic and alkaline media, the CO faradaic efficiency initially increased and then decreased with longer ligand side chains, whereas the C_{2+} product selectivity exhibited a non-

monotonic trend, first decreasing and then increasing as the side chain lengthened. Notably, the OMIm-Cu$_2$O catalyst demonstrated the best performance in both media, achieving a C$_{2+}$ selectivity of 63.3% under alkaline conditions (19% improvement) and 30.7% under acidic conditions (2.8-fold increase). Mechanistic investigations revealed that the long-chain imidazolium ligands enhance the hydrophobicity of the local microenvironment, thereby increasing the local *CO concentration and facilitating C$_2$ product formation.

2. Results and discussion

2.1 Characterization of Cu$_2$O@imidazole

We prepared the Cu$_2$O@imidazole sample *via* a ligand assisted wet chemistry method (details in ESI†). We first performed structural characterization of Cu$_2$O and Cu$_2$-O@imidazole *via* XRD. As shown in Fig. 1a, the diffraction peaks of Cu$_2$O and Cu$_2$O@imidazole align well with the standard cubic Cu$_2$O reference (PDF#00-005-0667), with no detectable impurity phases. Peaks observed at 29.5°, 36.4°, 42.3°, 61.3°, and 73.5° correspond to the (110), (111), (200), (220), and (311) planes of Cu$_2$O, respectively. Notably, Cu$_2$-O@imidazole retained identical diffraction patterns to Cu$_2$O, regardless of the alkyl chain length of the imidazolium ligands. This confirms that the surface modification preserves the crystalline structure of Cu$_2$O.

We conducted SEM and TEM to confirm the microstructure of Cu$_2$O@imidazole. The synthesized Cu$_2$O exhibited irregular nanoclusters with particle sizes ranging from 50 to 150 nm (Fig. S1†). Notably, Cu$_2$O@imidazole retained a similar
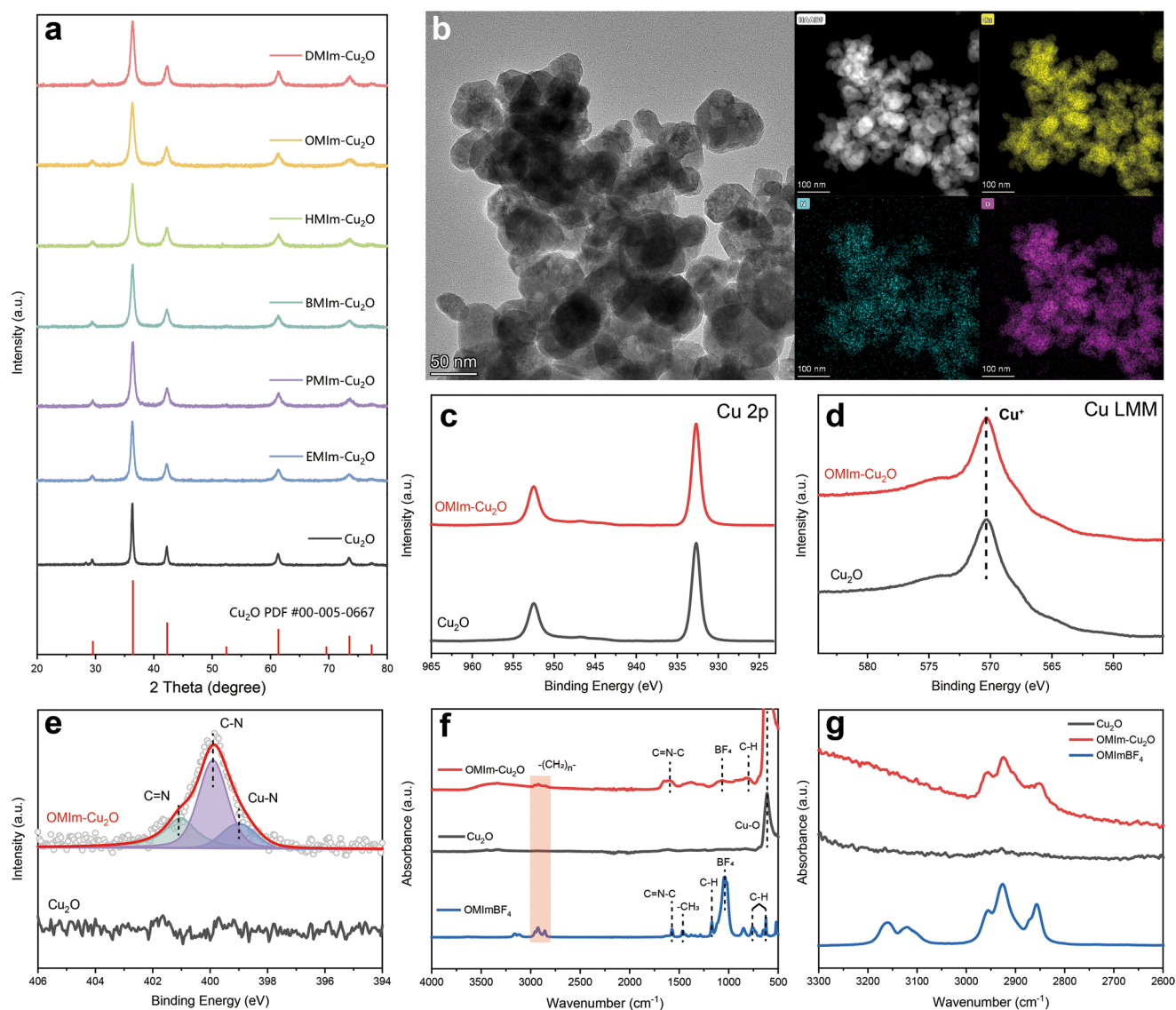
Fig. 1 (a) XRD patterns of the synthesized Cu$_2$O and Cu$_2$O@imidazole catalysts; (b) high-resolution TEM image of OMIm-Cu$_2$O, HAADF-STEM and EDS element mapping of OMIm-Cu$_2$O; (c) Cu 2p spectra of Cu$_2$O and OMIm-Cu$_2$O; (d) Cu LMM spectra of Cu$_2$O and OMIm-Cu$_2$O; (e) N 1s spectra of Cu$_2$O and OMIm-Cu$_2$O; (f) ATR-FTIR spectra of Cu$_2$O, OMIm-Cu$_2$O and OMIm-BF$_4$; (g) ATR-FTIR spectra of Cu$_2$O, OMIm-Cu$_2$O and OMIm-BF$_4$ enlarged in the range of 2600–3300 cm^{-1}.

morphology to Cu_2O without significant structural alterations (Fig. 1b). HRTEM image revealed distinct lattice spacings of 0.24 nm in Cu_2O, corresponding to the $Cu_2O(111)$ (PDF#00-005-0667). In contrast, the lattice spacing measured for OMIm-Cu_2O was 0.21 nm, which aligns with the $Cu_2O(200)$ (Fig. S2†). These showed excellent consistency with XRD pattern. HAADF-STEM coupled with EDS mapping demonstrated uniform distribution of Cu, O, and N elements on the OMIm-Cu_2O surface (Fig. 1b). The distinct presence of N provides direct evidence for the successful modification of imidazolium cations on the Cu_2O surface.

To investigate the chemical states of Cu_2O and Cu_2-O@imidazole, XPS measurements were performed. As shown in Fig. 1c, the Cu 2p spectra of both Cu_2O and OMIm-Cu_2O exhibited two distinct peaks at binding energies of 932.7 eV and 952.5 eV, corresponding to the Cu $2p_{3/2}$ and Cu $2p_{1/2}$ orbitals of Cu(I) or Cu(0), respectively. To further differentiate between Cu(I) and Cu(0), Cu LMM Auger spectra was conducted (Fig. 1d). It revealed a prominent peak at 570.3 eV, assigned to Cu(I). Notably, no significant differences were observed in the Cu 2p or Cu LMM spectra between Cu_2O and OMIm-Cu_2O, confirming the consistent presence of Cu(I) species, in agreement with XRD results. For the OMIm-Cu_2O catalyst, the N 1s spectrum (Fig. 1e) displayed three characteristic peaks: a peak at 399.0 eV attributed to Cu–N bonding,[19] and two additional peaks centered at 399.9 eV and 401.0 eV, corresponding to the C–N and C=N bonds in the imidazolium ring of OMIm-BF_4.[20,21] These confirm the successful anchoring of imidazolium on the Cu_2O. In contrast, no N 1s signal was detected in the same energy range for the Cu_2O sample.
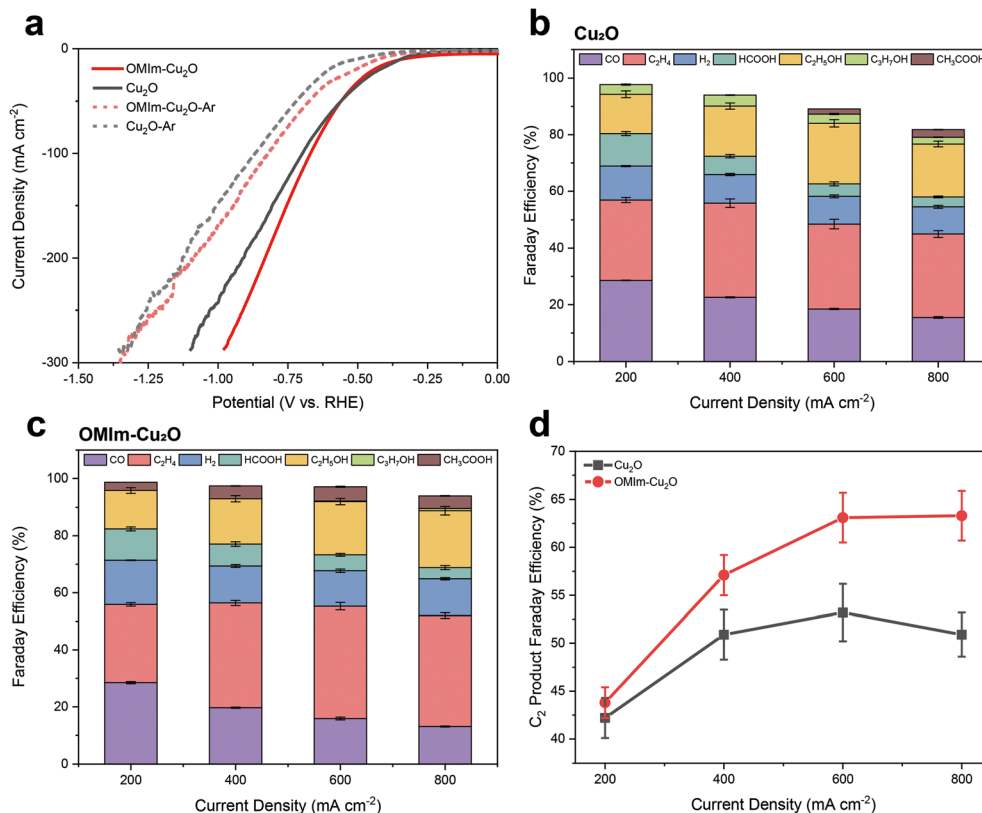
To confirm the presence of imidazolium molecular modification, ATR-FTIR was employed. The spectra of Cu_2O, OMIm-Cu_2O, and OMIm-BF_4 are shown in Fig. 1f. For Cu_2O, a single band at 610 cm^{-1} was observed, attributed to the Cu–O bond.[22,23] In contrast, the OMIm-Cu_2O spectrum retained the Cu–O stretching band at 610 cm^{-1} but exhibited additional peaks at 810, 1080, 1600, 2900, and 3340 cm^{-1}. The broad peak at 3340 cm^{-1} corresponds to O–H stretching vibrations from adsorbed water, while the remaining bands are associated with the surface-bound imidazolium molecular layer. For comparison, OMIm-BF_4 exhibited characteristic vibrational bands: the strongest peak at 1080 cm^{-1} was assigned to the BF_4^- anion,[24,25] the C=C–N in-plane stretching vibration of the imidazolium ring appeared at 1570 cm^{-1},[26] the symmetric stretching vibration of –CH_3 on the imidazolium ring was observed at 1468 cm^{-1},[27,28] and peaks at 1167, 750, and 620 cm^{-1} originated from C–H of the imidazolium ring.[27,29] These imidazolium-related peaks were also detected at analogous positions in the OMIm-Cu_2O. Crucially, the methylene C–H stretching vibrations (2800–3000 cm^{-1}) of the octyl chain in OMIm-BF_4 were prominently retained in OMIm-Cu_2O (Fig. 1g).[30] These results provide conclusive evidence for the successful modification of the Cu_2O surface with imidazolium.

2.2 CO_2RR performance

We firstly investigated the CO_2 reduction performance of Cu_2-O@Imidazole in 1 M KOH electrolyte. We analyzed the gas products by an online gas chromatography (GC) and the liquid products by a nuclear magnetic resonance (NMR). The LSV curves in Fig. 2a demonstrate that both Cu_2O and OMIm-Cu_2O exhibit significantly higher activity for CO_2RR than HER. While the onset potentials for CO_2RR were comparable between OMIm-Cu_2O and Cu_2O, the OMIm-Cu_2O displayed a steeper slope, suggesting enhanced activity due to the imidazolium ligands. Product selectivity at varying current densities (200–800 mA cm^{-2}) are presented in Fig. 2b and c. For Cu_2O, CO and C_2H_4 dominated the product distribution (Fig. 2b). The CO selectivity peaked at 28.6% at 200 mA cm^{-2} but progressively decreased with higher current densities. Concurrently, C_{2+} product selectivity for Cu_2O measured 42.2%, 50.9%, 53.2%, and 50.9% at 200, 400, 600, and 800 mA cm^{-2}, respectively. In contrast, the imidazolium-functionalized OMIm-Cu_2O catalyst achieved substantially enhanced C_{2+} product selectivity of 43.8%, 57.1%, 63.1%, and 63.3% under identical conditions (Fig. 2c and d). This systematic improvement across all tested current densities underscores the critical role of imidazolium modification in promoting multi-carbon product formation.

A series of Cu_2O@imidazole catalysts with varying alkyl chain lengths were synthesized, including ethyl (EMIm-Cu_2O), propyl (PMIm-Cu_2O), butyl (BMIm-Cu_2O), hexyl (HMIm-Cu_2O), octyl (OMIm-Cu_2O), and decyl (DMIm-Cu_2O), with alkyl chains ranging from 2 to 10 carbons. Their CO_2RR performance under alkaline conditions was systematically evaluated (Fig. 3a and b). The alkyl chain length exerted a pronounced influence on product selectivity, revealing distinct trends. As shown in Fig. 3a, CO selectivity exhibited a volcano-shaped dependence on chain length. BMIm-Cu_2O (n = 4) achieved the highest CO selectivity of 64.6% at 200 mA cm^{-2}, representing a 2.25-fold enhancement compared to Cu_2O. In contrast, C_{2+} product selectivity displayed an inverse trend, initially decreasing and then increasing with chain elongation. For shorter chains (n = 2, 3, 4), EMIm-Cu_2O, PMIm-Cu_2O, and BMIm-Cu_2O showed lower C_{2+} selectivity than Cu_2O, with values diminishing as chain length increased. However, catalysts with longer alkyl chains (n = 6, 8, 10) reversed this trend, HMIm-Cu_2O, OMIm-Cu_2O, and DMIm-Cu_2O demonstrating progressively higher C_{2+} selectivity. Notably, OMIm-Cu_2O (n = 8) achieved the highest C_{2+} selectivity of 63.3% at 600 mA cm^{-2}, underscoring the critical role of chain length in modulating multi-carbon product formation. A comparative analysis of key metrics (*e.g.*, FE, partial current density) between OMIm-Cu_2O and literature-reported imidazolium ligand-modified electrocatalysts (Table S1†) further confirms its state-of-the-art performance in C_{2+} production. Furthermore, stability tests of the optimal OMIm-Cu_2O catalyst at 600 mA cm^{-2} revealed sustained performance over 6 hours, though gradual activity decay was observed (Fig. S3†). Post-stability

© 2025 The Author(s). Co-published by the Institute of Process Engineering, Chinese Academy of Sciences and the Royal Society of Chemistry

Ind. Chem. Mater., 2025, **3**, 431–439 | **433**

Fig. 2 CO_2RR performance of Cu_2O and $OMIm-Cu_2O$ under alkaline conditions. (a) LSV curves of Cu_2O and $OMIm-Cu_2O$ in CO_2 and Ar; (b) product faraday efficiency of Cu_2O during CO_2RR at different applied current densities; (c) product Faraday efficiency of $OMIm-Cu_2O$ during CO_2RR at different applied current densities; (d) C_{2+} FE of $OMIm-Cu_2O$ and Cu_2O at different current densities.

characterization indicated that morphological degradation and imidazolium ligand detachment may contribute to this decline (Fig. S4†).

Under acidic conditions, the imidazolium ligand modification similarly influenced product selectivity. To effectively suppress the HER in acidic media, a high-concentration potassium ion environment was employed using 3 M KCl electrolyte acidified to pH = 1 with HCl. The product FE for Cu_2O and $OMIm-Cu_2O$ under acidic electrolyte are shown in Fig. S5.† For Cu_2O, H_2 dominated as the primary product, with a selectivity of 51% at 200 mA cm^{-2}. Remarkably, for $OMIm-Cu_2O$, imidazolium modification significantly suppressed HER, reducing H_2 selectivity to 19.3% and 16.9% at 100 and 200 mA cm^{-2}, respectively. Additionally, the imidazolium modification completely inhibited CH_4 formation, in stark contrast to Cu_2O.

Similar to alkaline conditions, variations in alkyl chain length induced systematic trends in acidic CO_2RR FE. As depicted in Fig. 3c, CO FE also followed a volcano-shaped dependence on chain length, peaking at 51.3% for HMIm-Cu_2O (n = 6) at 200 mA cm^{-2}. HMIm-Cu_2O obtained a 2.3-fold enhancement over unmodified Cu_2O. For C_{2+} products, selectivity mirrored the alkaline trend, initially decreasing and then increasing with chain elongation. $OMIm-Cu_2O$ (n = 8) achieved the highest C_{2+} selectivity of 30.7% at 200 mA cm^{-2} under acidic conditions,

representing a 2.8-fold improvement compared to Cu_2O Fig. 3d. These results highlight the dual role of imidazolium ligands in acidic media: suppressing parasitic HER/CH_4 while promoting CO and C_2 pathways, with alkyl chain length serving as a critical modulator of interfacial reactivity.

2.3 Mechanism study

The experimental data conclusively demonstrate the critical role of imidazolium ligand side-chain length in regulating CO_2RR product selectivity. To elucidate the mechanistic origins of this enhancement, we investigated the interfacial microenvironment and dynamic structural effects through *in situ* ATR-SEIRAS. Fig. 4 and S6† displays the spectra of interfacial water for Cu_2O, $BMIm-Cu_2O$ and $OMIm-Cu_2O$ during CO_2RR. Gaussian fitting of the spectra reveals that the O–H stretching vibration peaks of interfacial water (Fig. 4a, b and S6) can be deconvoluted into three distinct components, corresponding to three types of O–H stretching vibrations: isolated water molecules (~3570 cm^{-1}, purple peaks), asymmetric H-bonded water (~3400 cm^{-1}, yellow peaks), and ice-like water (~3220 cm^{-1}, red peaks). The proportional distribution of these three water configurations on the catalyst surface was quantified through relative peak area analysis (Fig. 4c).
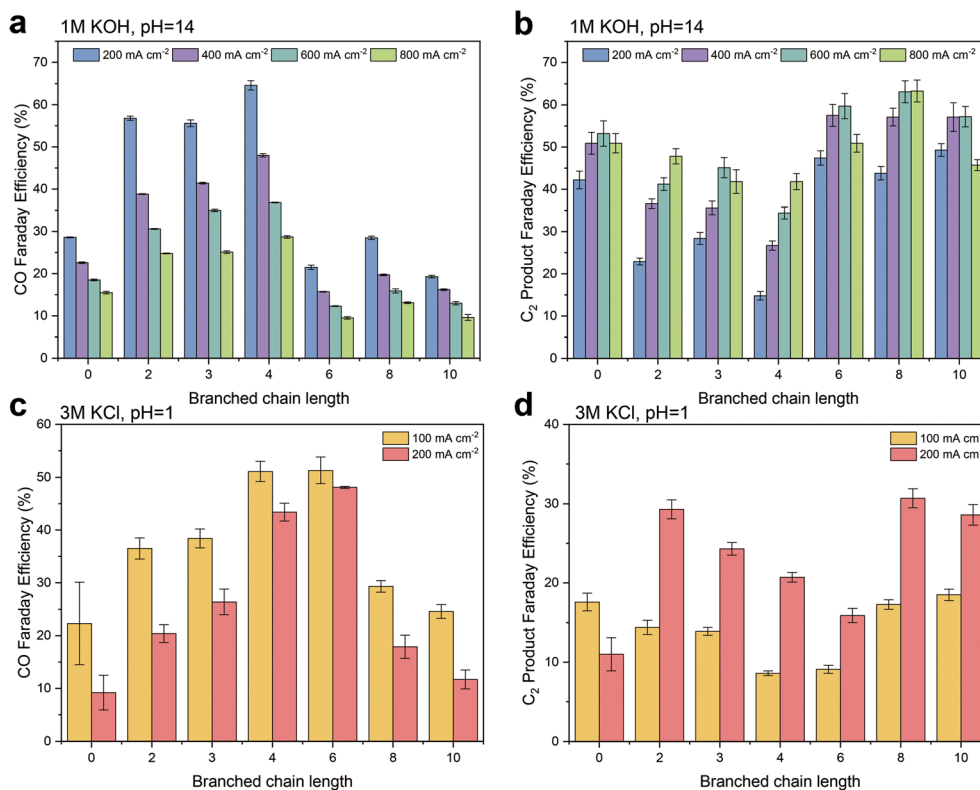
Fig. 3 Effects of imidazolium ligands with different branch lengths on product selectivity. (a) Relationship between imidazolium ligand branch length and CO selectivity under alkaline conditions; (b) relationship between imidazolium ligand branch length and C_{2+} product selectivity under alkaline conditions; (c) relationship between imidazolium ligand branch length and CO selectivity under acidic conditions; (d) relationship between imidazolium ligand branch length and C_{2+} product selectivity under acidic conditions.
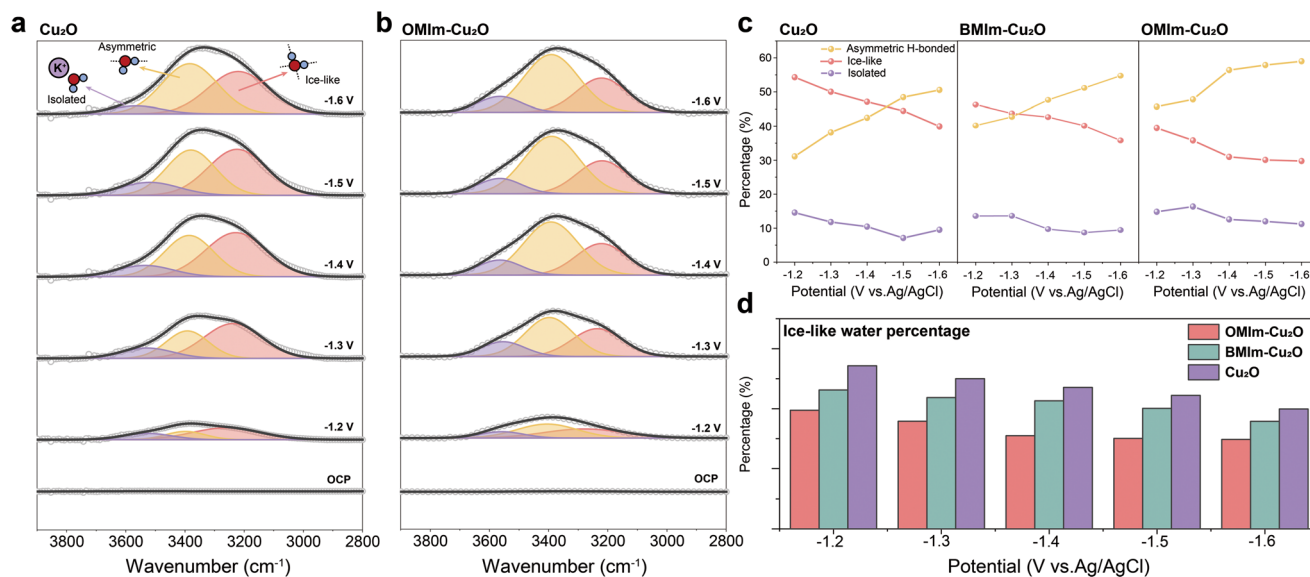
Fig. 4 Regulation of the H_2O hydrogen-bonding network after imidazolium ligands modification. (a) In situ ATR-SEIRAS spectra of interfacial H_2O during CO_2RR on a Cu_2O electrode in 1 M $KHCO_3$; (b) in situ ATR-SEIRAS spectra of interfacial H_2O during CO_2RR on an OMIm-Cu_2O electrode in 1 M $KHCO_3$. Gaussian fits of the three O–H stretching modes are shown in purple, orange, and red, respectively; (c) the ratio of the three water peaks at the interface between Cu_2O, BMIm-Cu_2O and OMIm-Cu_2O during CO_2RR, obtained from the peak area ratio after Gaussian fitting; (d) the ratio of ice-like water at different potentials at the interface between Cu_2O, BMIm-Cu_2O and OMIm-Cu_2O.

Notably, the hydrogen-bonding structure of interfacial water undergoes significant changes with increasing applied potential: the proportion of asymmetric H-bonded water increases markedly while ice-like water decreases. The

© 2025 The Author(s). Co-published by the Institute of Process Engineering, Chinese Academy of Sciences and the Royal Society of Chemistry

Ind. Chem. Mater., 2025, 3, 431–439 | 435

reduction in ice-like water (the predominant configuration in bulk solvent) suggests electric field-induced enrichment of metal cations at the catalyst surface and subsequent reorganization of interfacial water distribution. However, imidazolium-modified BMIm-Cu_2O and OMIm-Cu_2O exhibits further enhancement in asymmetric H-bonded water and greater suppression of ice-like water compared to unmodified Cu_2O across all potentials (Fig. 4c and d). This phenomenon aligns with previous reports demonstrating that flexible alkyl chains of organic ligands undergo electric field-regulated structural reorganization at solid–liquid interfaces.[31–35] The observed decrease in ice-like water and concurrent increase in asymmetric H-bonded water confirm similar ordering processes on BMIm-Cu_2O and OMIm-Cu_2O surfaces.[31] The imidazolium ligand modification regulated the microenvironment. The long alkyl chains in the ligand layer undergo spontaneous self-organization, forming a structured molecular arrangement that effectively reduces water molecule density at the interfacial region. This ultimately constructs a gradient hydrophobic–aerophilic microenvironment at the electrochemical interface. Moreover, the percentage of ice-like water at the electrode–electrolyte interface decreases monotonically with increasing alkyl chain length, demonstrating the regulatory role of alkyl chain length in modulating the hydrophobicity balance within the local microenvironment.

Next, we estimated the ECSA of Cu_2O and OMIm-Cu_2O. The calculated C_{dl} for Cu_2O and OMIm-Cu_2O were 1.57 and 1.60 mF cm^{-2}, respectively, indicating comparable ECSA

values between the two catalysts (Fig. S7†). To investigate the influence of imidazolium modification on charge transfer properties, we conducted EIS measurements for Cu_2O and OMIm-Cu_2O (Fig. S7†). At lower potentials, OMIm-Cu_2O exhibited a similar R_{ct} to that of Cu_2O. However, with increasing potential, the R_{ct} of OMIm-Cu_2O became significantly reduced compared to Cu_2O, demonstrating that the imidazolium ligand modification substantially enhances charge transfer capability at elevated working potentials.

Subsequently, we employed *in situ* ATR-SEIRAS to monitor the evolution of surface-active intermediates during CO_2RR. As shown in Fig. 5a, b and S8,† the peak at ~1500 cm^{-1} observed on Cu_2O, BMIm-Cu_2O and OMIm-Cu_2O corresponds to the symmetric O–C–O stretching vibration of adsorbed *COO^-,[36] indicating CO_2 adsorption and accumulation at low potentials. This intermediate diminishes progressively as the potential increases, consistent with its transformation into downstream species. Concurrently, the emergence of *CO intermediates in the 2000–2100 cm^{-1} range at intermediate potentials suggests hydrogenation of *COO^- to *CO, a critical branching point for product selectivity.[36,37] Notably, at higher potentials, OMIm-Cu_2O exhibits significantly weaker signals at ~1450 cm^{-1} and ~1350 cm^{-1} compared to Cu_2O and BMIm-Cu_2O (Fig. 5d), which are assigned to *OCCHO species formed through C–C coupling.[36] This observation aligns with the enhanced C_{2+} selectivity of OMIm-Cu_2O.

The *CO peaks at 2080–2100 cm^{-1} exhibit Stark shifts (Fig. 5e), where the Stark tuning rate—primarily influenced by intermediate coverage—serves as an indicator of the *CO
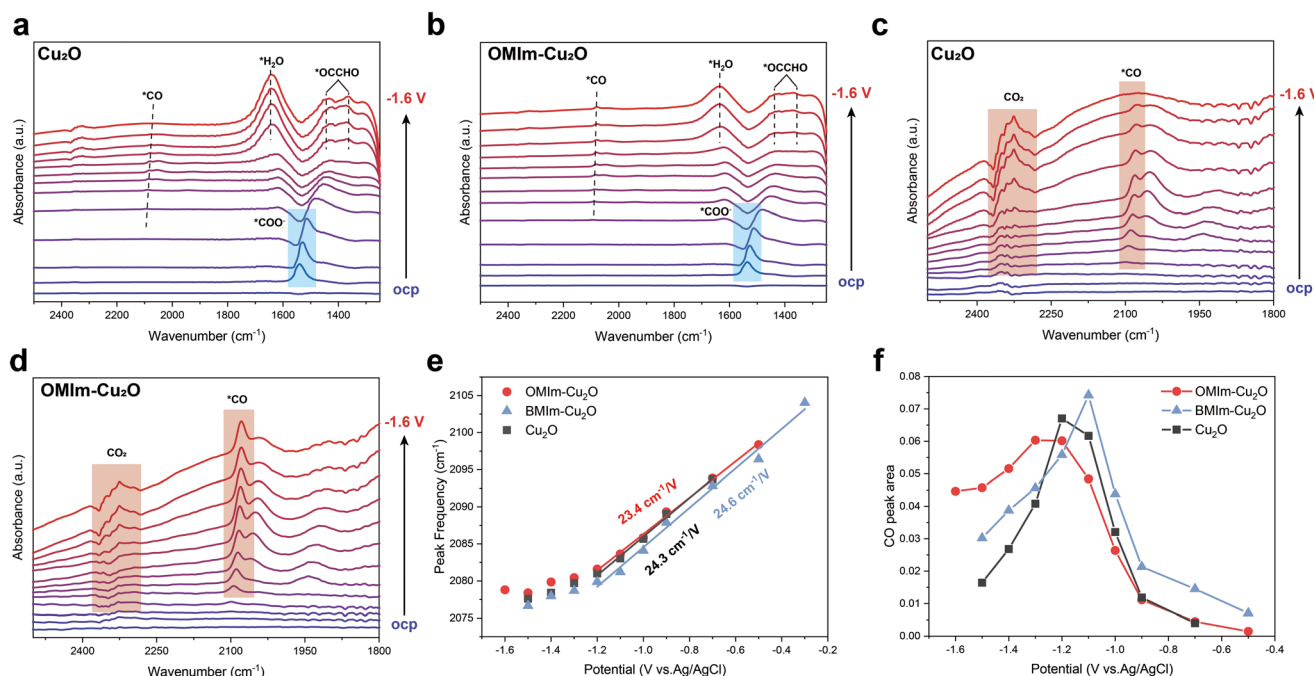
Fig. 5 Mechanistic study on the enhanced CO_2RR performance by imidazolium surface modification. *In situ* ATR-SEIRAS spectra of (a) Cu_2O and (b) OMIm-Cu_2O in CO_2-saturated 1 M KHCO$_3$ electrolyte; (c) magnified *in situ* ATR-SEIRAS spectra of Cu_2O and (d) OMIm-Cu_2O in the range of 2500–1800 cm^{-1}; (e) variation of *CO peak position with potential for Cu_2O, BMIm-Cu_2O and OMIm-Cu_2O. The Stark shift frequency was determined by linear fitting; (f) relationship between *CO peak area on the surface of Cu_2O, BMIm-Cu_2O and OMIm-Cu_2O and applied potential.

adsorption capacity.[38–40] Notably, Cu_2O, $BMIm-Cu_2O$ and $OMIm-Cu_2O$ display comparable Stark tuning rates (24.3, 24.6, and 23.4 cm^{-1} V^{-1}), demonstrating that imidazolium modification does not alter the intrinsic *CO adsorption capability of Cu_2O. Both catalysts show an initial increase followed by a decrease in *CO peak area with increasing potential. However, $BMIm-Cu_2O$ retains higher *CO concentrations than unmodified Cu_2O at higher potentials (>1.3 V *vs.* Ag/AgCl), though slightly lower than $OMIm-Cu_2O$ (Fig. 5f). This trend aligns with the increasement of alkyl chain length, directly linking longer alkyl chains to enhanced CO retention. This potential-dependent behavior arises from competing processes: while *CO accumulation dominates at lower potentials, its depletion at higher potentials results from C–C coupling of *CO intermediates. The sustained high *CO concentration on $OMIm-Cu_2O$ under high potentials reveals that imidazolium modification enhances local *CO coverage. These findings elucidate the optimization mechanism of imidazolium ligands for CO_2RR: The hydrophobic–aerophilic microenvironment constructed by long-chain imidazolium ligands elevates local *CO concentrations at the catalyst interface, particularly under high-potential conditions. This enriched *CO coverage facilitates C–C coupling kinetics, thereby improving C_{2+} product selectivity.

3. Conclusions

This study demonstrates that tailoring the alkyl chain length of imidazolium ligands enables microenvironment modulation for optimizing CO_2RR selectivity on Cu_2O catalysts. Structural analysis confirms the stable anchoring of imidazolium molecules *via* Cu–N coordination without altering the Cu_2O structure. A volcano-shaped dependence of CO selectivity on alkyl chain length is observed, with $BMIm-Cu_2O$ (C_4) and $HMIm-Cu_2O$ (C_6) achieving 2.25- and 2.3-fold enhancements in CO FE under alkaline and acidic conditions. Remarkably, hydrophobic alkyl chains suppress hydrogen evolution and completely inhibit CH_4 formation. Mechanistically, the alkyl side chains form an electric field-induced hydrophobic layer, reducing interfacial ice-like water content by 10.1–14.8%, thereby enriching local *CO intermediates. *In situ* ATR-SEIRAS evidence corroborates that this microenvironment facilitates *CO retention and C–C coupling, rationalizing the enhanced C_{2+} selectivity. These findings underscore the critical role of ligand-engineered microenvironments in steering CO_2RR pathways.

4. Experimental section

4.1 Synthesis of Cu_2O

First, 2.0 g of anhydrous sodium tetraborate ($Na_2B_4O_7$) was added to 70 mL of hot deionized water (90 °C) under continuous magnetic stirring for over 10 minutes to ensure complete dissolution, yielding a clear and homogeneous solution. After cooling the sodium tetraborate solution to room temperature, 0.8 g of sodium ascorbate was introduced into the mixture under vigorous stirring. The stirring was maintained for an additional 10 minutes, followed by the addition of 0.4 g of $CuCl_2$. Upon incorporation of $CuCl_2$, the solution immediately transitioned to an orange-yellow coloration. After 7 minutes of reaction, the resulting product was isolated *via* centrifugation, thoroughly washed with deionized water, and subsequently vacuum-dried at 60 °C for 12 hours.

4.2 Synthesis of Cu_2O@imidazole

Catalysts modified with imidazolium of varying alkyl chain lengths (C_2–C_{10}) were designated as $EMIm-Cu_2O$, $PMIm-Cu_2O$, $BMIm-Cu_2O$, $HMIm-Cu_2O$, $OMIm-Cu_2O$, and $DMIm-Cu_2O$, respectively. Take the synthesis of $EMIm-Cu_2O$ as an example: first, 2.0 g of anhydrous sodium tetraborate ($Na_2B_4-O_7$) was dissolved in 70 mL of hot deionized water (90 °C) under magnetic stirring for at least 10 minutes to form a clear solution. After cooling the solution to room temperature, 0.8 g of sodium ascorbate and 0.1 g of 1-ethyl-3-methylimidazolium tetrafluoroborate ($EMImBF_4$) were added sequentially to the sodium tetraborate solution under vigorous stirring. The mixture was stirred continuously for 10 minutes, followed by the addition of 0.4 g of $CuCl_2$. Upon introducing $CuCl_2$, the solution rapidly turned orange-yellow. After 7 minutes, the product was collected *via* centrifugation, washed repeatedly with deionized water, and vacuum-dried at 60 °C for 12 hours. The synthesis procedures for $PMIm-Cu_2O$, $BMIm-Cu_2O$, $HMIm-Cu_2O$, $OMIm-Cu_2O$, and $DMIm-Cu_2O$ were identical to that of $EMIm-Cu_2O$, except that $EMImBF_4$ was replaced with the corresponding imidazolium salts: $PMImBF_4$ (1-propyl-3-methylimidazolium tetrafluoroborate), $BMImBF_4$ (1-butyl-3-methylimidazolium tetrafluoroborate), $HMImBF_4$ (1-hexyl-3-methylimidazolium tetrafluoroborate), $OMImBF_4$ (1-octyl-3-methylimidazolium tetrafluoroborate), $DMImBF_4$ (1-decyl-3-methylimidazolium tetrafluoroborate).

Data availability

The data supporting this article have been included as part of the ESI.†

Conflicts of interest

The authors declare no conflict of interest.

Acknowledgements

© 2025 The Author(s). Co-published by the Institute of Process Engineering, Chinese Academy of Sciences and the Royal Society of Chemistry

Ind. Chem. Mater., 2025, **3**, 431–439 | **437**

References

1 Z. Sun, Y. Hu, D. Zhou, M. Sun, S. Wang and W. Chen, Factors influencing the performance of copper-bearing catalysts in the CO_2 reduction system, *ACS Energy Lett.*, 2021, **6**, 3992–4022.

2 X. Zhi, Y. Jiao, Y. Zheng, K. Davey and S.-Z. Qiao, Directing the selectivity of CO_2 electroreduction to target C_2 products via non-metal doping on Cu surfaces, *J. Mater. Chem. A*, 2021, **9**, 6345–6351.

3 Z. Gu, H. Shen, Z. Chen, Y. Yang, C. Yang, Y. Ji, Y. Wang, C. Zhu, J. Liu, J. Li, T.-K. Sham, X. Xu and G. Zheng, Efficient electrocatalytic CO_2 reduction to C_{2+} alcohols at defect-site-rich Cu surface, *Joule*, 2021, **5**, 429–440.

4 Z.-Z. Niu, F.-Y. Gao, X.-L. Zhang, P.-P. Yang, R. Liu, L.-P. Chi, Z.-Z. Wu, S. Qin, X. Yu and M.-R. Gao, Hierarchical copper with Inherent hydrophobicity mitigates electrode flooding for high-rate CO_2 electroreduction to multicarbon products, *J. Am. Chem. Soc.*, 2021, **143**, 8011–8021.

5 H. Huo, J. Wang, Q. Fan, Y. Hu and J. Yang, Cu-MOFs derived porous Cu nanoribbons with strengthened electric field for selective CO_2 electroreduction to C_{2+} fuels, *Adv. Energy Mater.*, 2021, **11**, 2102447.

6 C. Peng, G. Luo, Z. Xu, S. Yan, J. Zhang, M. Chen, L. Qian, W. Wei, Q. Han and G. Zheng, Lithiation-enabled high-density nitrogen vacancies electrocatalyze CO_2 to C_2 products, *Adv. Mater.*, 2021, **33**, 2103150.

7 M. Li, Y. Ma, J. Chen, R. Lawrence, W. Luo, M. Sacchi, W. Jiang and J. Yang, Residual chlorine induced cationic active species on a porous copper electrocatalyst for highly stable electrochemical CO_2 reduction to C_{2+}, *Angew. Chem.*, 2021, **60**, 11487–11493.

8 Z. Lyu, S. Zhu, M. Xie, Y. Zhang, Z. Chen, R. Chen, M. Tian, M. Chi, M. Shao and Y. Xia, Controlling the surface oxidation of Cu nanowires improves their catalytic selectivity and stability toward C_{2+} products in CO_2 reduction, *Angew. Chem., Int. Ed.*, 2021, **60**, 1909–1915.

9 C. Liu, J. Gong, J. Li, J. Yin, W. Li, Z. Gao, L. Xiao, G. Wang, J. Lu and L. Zhuang, Preanodized Cu surface for selective CO_2 electroreduction to C_1 or C_{2+} products, *ACS Appl. Mater. Interfaces*, 2022, **14**, 20953–20961.

10 K. D. Yang, W. R. Ko, J. H. Lee, S. J. Kim, H. Lee, M. H. Lee and K. T. Nam, Morphology-directed selective production of ethylene or ethane from CO_2 on a Cu mesopore electrode, *Angew. Chem., Int. Ed.*, 2017, **56**, 796–800.

11 C. Kim, K. M. Cho, K. Park, J. Y. Kim, G.-T. Yun, F. M. Toma, I. Gereige and H.-T. Jung, Cu/Cu_2O interconnected porous aerogel catalyst for highly productive electrosynthesis of ethanol from CO_2, *Adv. Funct. Mater.*, 2021, **31**, 2102142.

12 Z. Cao, S. B. Zacate, X. Sun, J. Liu, E. M. Hale, W. P. Carson, S. B. Tyndall, J. Xu, X. Liu, X. Liu, C. Song, J.-h. Luo, M.-J. Cheng, X. Wen and W. Liu, Tuning gold nanoparticles with chelating ligands for highly efficient electrocatalytic CO_2 reduction, *Angew. Chem., Int. Ed.*, 2018, **57**, 12675–12679.

13 Y. Yang, C. Zhang, C. Zhang, Y. Shi, J. Li, B. Johannessen, Y. Liang, S. Zhang, Q. Song, H. Zhang, J. Huang, J. Ke, L. Zhang, Q. Song, J. Zeng, Y. Zhang, Z. Geng, P.-S. Wang, Z. Wang, J. Zeng and F. Li, Ligand-tuning copper in coordination polymers for efficient electrochemical C–C coupling, *Nat. Commun.*, 2024, **15**, 6316.

14 D. Qin, S. Song, Y. Liu, K. Wang, B. Yang and S. Zhang, Enhanced electrochemical nitrate-to-ammonia performance of cobalt oxide by protic ionic liquid modification, *Angew. Chem., Int. Ed.*, 2023, **62**, e202304935.

15 Y. Chen, X. Zhou, X. Liu, Z. Tang, L. Wang and Q. Tang, Understanding the role of potential and cation effect on electrocatalytic CO_2 reduction in all-alkynyl-protected Ag_{15} nanoclusters, *J. Am. Chem. Soc.*, 2025, **147**, 2699–2713.

16 H. Zhang, C. Xu, X. Zhan, Y. Yu, K. Zhang, Q. Luo, S. Gao, J. Yang and Y. Xie, Mechanistic insights into CO_2 conversion chemistry of copper bis-(terpyridine) molecular electrocatalyst using accessible operando spectrochemistry, *Nat. Commun.*, 2022, **13**, 6029.

17 J. J. Clerix, A. Sanz-Matias, S. Armini, J. N. Harvey and A. Delabie, Structural phases of alkanethiolate self-assembled monolayers (C1–12) on Cu[100] by density functional theory, *J. Phys. Chem. C*, 2020, **124**, 3802–3811.

18 J. Fu, W. Zhu, Y. Chen, Z. Yin, Y. Li, J. Liu, H. Zhang, J.-J. Zhu and S. Sun, Bipyridine-assisted assembly of Au nanoparticles on Cu nanowires to enhance the electrochemical reduction of CO_2, *Angew. Chem., Int. Ed.*, 2019, **58**, 14100–14103.

19 H. Cheng, X. Wu, X. Li, X. Nie, S. Fan, M. Feng, Z. Fan, M. Tan, Y. Chen and G. He, Construction of atomically dispersed $Cu-N_4$ sites via engineered coordination environment for high-efficient CO_2 electroreduction, *Chem. Eng. J.*, 2021, **407**, 126842.

20 Z. Li, W. Wang, Y. Chen, C. Xiong, G. He, Y. Cao, H. Wu, M. D. Guiver and Z. Jiang, Constructing efficient ion nanochannels in alkaline anion exchange membranes by the in situ assembly of a poly(ionic liquid) in metal–organic frameworks, *J. Mater. Chem. A*, 2016, **4**, 2340–2348.

21 Y. Sha, J. Zhang, X. Cheng, M. Xu, Z. Su, Y. Wang, J. Hu, B. Han and L. Zheng, Anchoring ionic liquid in copper electrocatalyst for improving CO_2 conversion to ethylene, *Angew. Chem., Int. Ed.*, 2022, **61**, e202200039.

22 V. Sudha, G. Murugadoss and R. Thangamuthu, Structural and morphological tuning of Cu-based metal oxide nanoparticles by a facile chemical method and highly electrochemical sensing of sulphite, *Sci. Rep.*, 2021, **11**, 3413.

23 N. Zayyoun, L. Bahmad, L. Laânab and B. Jaber, The effect of pH on the synthesis of stable Cu_2O/CuO nanoparticles by sol–gel method in a glycolic medium, *Appl. Phys. A: Mater. Sci. Process.*, 2016, **122**, 488.

24 A. Dong, X. Ye, J. Chen, Y. Kang, T. Gordon, J. M. Kikkawa and C. B. Murray, A generalized ligand-exchange strategy enabling sequential surface functionalization of colloidal nanocrystals, *J. Am. Chem. Soc.*, 2011, **133**, 998–1006.

25 S. Y. Kottsov, G. P. Kopitsa, A. E. Baranchikov, A. A. Pavlova, T. V. Khamova, A. O. Badulina, Y. E. Gorshkova, N. A. Selivanov, N. P. Simonenko, M. E. Nikiforova and V. K. Ivanov, Structural insight into ionogels: A case study of

1-methyl-3-octyl-imidazolium tetrafluoroborate confined in aerosil, *Langmuir*, 2024, **40**, 23962–23972.

26 E. Navarrete-Astorga, J. Rodríguez-Moreno, E. A. Dalchiele, R. Schrebler, P. Leyton, J. R. Ramos-Barrado and F. Martín, A transparent solid-state ion gel for supercapacitor device applications, *J. Solid State Electrochem.*, 2017, **21**, 1431–1444.

27 J. Jiang, D. Gao, Z. Li and G. Su, Gel polymer electrolytes prepared by in situ polymerization of vinyl monomers in room-temperature ionic liquids, *React. Funct. Polym.*, 2006, **66**, 1141–1148.

28 J. A. Collado, I. Tuñón, E. Silla and F. J. Ramírez, Vibrational dynamics of histamine monocation in solution: an experimental (FT-IR, FT-Raman) and theoretical (SCRF-DFT) study, *J. Phys. Chem. A*, 2000, **104**, 2120–2131.

29 N. Nanbu, Y. Sasaki and F. Kitamura, In situ FT-IR spectroscopic observation of a room-temperature molten salt|gold electrode interphase, *Electrochem. Commun.*, 2003, **5**, 383–387.

30 J. Rodríguez, E. Navarrete, E. A. Dalchiele, L. Sánchez, J. R. Ramos-Barrado and F. Martín, Polyvinylpyrrolidone–$LiClO_4$ solid polymer electrolyte and its application in transparent thin film supercapacitors, *J. Power Sources*, 2013, **237**, 270–276.

31 W. Ge, Y. Chen, Y. Fan, Y. Zhu, H. Liu, L. Song, Z. Liu, C. Lian, H. Jiang and C. Li, Dynamically formed surfactant assembly at the electrified electrode–electrolyte interface boosting CO_2 electroreduction, *J. Am. Chem. Soc.*, 2022, **144**, 6613–6622.

32 E. Shirzadi, Q. Jin, A. S. Zeraati, R. Dorakhan, T. J. Goncalves, J. Abed, B.-H. Lee, A. S. Rasouli, J. Wicks, J. Zhang, P. Ou, V. Boureau, S. Park, W. Ni, G. Lee, C. Tian, D. M. Meira, D. Sinton, S. Siahrostami and E. H. Sargent, Ligand-modified nanoparticle surfaces influence CO electroreduction selectivity, *Nat. Commun.*, 2024, **15**, 2995.

33 X. Kong, J. Zhu, Z. Xu and Z. Geng, Fundamentals and challenges of ligand modification in heterogeneous electrocatalysis, *Angew. Chem.*, 2025, **64**, e202417562.

34 D. Kim, S. Yu, F. Zheng, I. Roh, Y. Li, S. Louisia, Z. Qi, G. A. Somorjai, H. Frei, L.-W. Wang and P. Yang, Selective CO_2 electrocatalysis at the pseudocapacitive nanoparticle/ordered-ligand interlayer, *Nat. Energy*, 2020, **5**, 1032–1042.

35 L. Xiao, X. Zheng, J. Bai, J. Tan, D. Meng, Z. Zhang, H. Liu, L. Gong, S. Luo, S. Ye, Z. Jiang, L. Shan and S. Zhang, Ordered interfacial water generated at poly(ionic liquid) membrane surface imparts ultrafast water transport and superoleophobicity, *J. Am. Chem. Soc.*, 2025, **147**, 3507–3516.

36 E. P. Delmo, Y. Wang, Y. Song, S. Zhu, H. Zhang, H. Xu, T. Li, J. Jang, Y. Kwon, Y. Wang and M. Shao, In situ infrared spectroscopic evidence of enhanced electrochemical CO_2 reduction and C–C coupling on oxide-derived copper, *J. Am. Chem. Soc.*, 2024, **146**, 1935–1945.

37 N. J. Firet and W. A. Smith, Probing the reaction mechanism of CO_2 electroreduction over Ag films via operando infrared spectroscopy, *ACS Catal.*, 2017, **7**, 606–612.

38 R. M. Hammaker, S. A. Francis and R. P. Eischens, Infrared study of intermolecular interactions for carbon monoxide chemisorbed on platinum, *Spectrochim. Acta*, 1965, **21**, 1295–1309.

39 J. Uddin and A. B. Anderson, Trends with coverage and pH in Stark tuning rates for CO on Pt(111) electrodes, *Electrochim. Acta*, 2013, **108**, 398–403.

40 P. Hollins and J. Pritchard, Infrared studies of chemisorbed layers on single crystals, *Prog. Surf. Sci.*, 1985, **19**, 275–349.

© 2025 The Author(s). Co-published by the Institute of Process Engineering, Chinese Academy of Sciences and the Royal Society of Chemistry

Ind. Chem. Mater., 2025, **3**, 431–439 | **439**